COMPUTER METHODS IN APPLIED MECHANICS AND ENGINEERING 61 (1987) 189–214
NORTH-HOLLAND

A FINITE ELEMENT METHOD FOR LOCALIZED FAILURE ANALYSIS*

Michael ORTIZ, Yves LEROY and Alan NEEDLEMAN
Division of Engineering, Brown University, Providence, RI 02912, U.S.A.

Received 9 April 1986

A method is proposed which aims at enhancing the performance of general classes of elements in problems involving strain localization. The method exploits information concerning the process of localization which is readily available at the element level. A bifurcation analysis is used to determine the geometry of the localized deformation modes. When the onset of localization is detected, suitably defined shape functions are added to the element interpolation which closely reproduce the localized modes. The extra degrees of freedom representing the amplitudes of these modes are eliminated by static condensation. The proposed methodology can be applied to 2-D and 3-D problems involving arbitrary rate-independent material behavior. Numerical examples demonstrate the ability of the method to resolve the geometry of localized failure modes to the highest resolution allowed by the mesh.

1. Introduction

A phenomenon that frequently accompanies inelastic deformation is the formation of localized bands of intense straining. This phenomenon of localization occurs in a wide variety of solids; in ductile single crystals [1], in structural metals [2, 3], in saturated clays [4, 5], in rocks [6], and in concrete [7]. The physical mechanisms responsible for triggering localization vary widely. For example, at high rates of loading in structural metals, thermal softening plays a key role in initiating localization [2]. Localization also occurs in metals at low rates of loading, where thermal effects are negligible [1, 3]. Once localization takes place, large strains can accumulate inside the band and lead to fracture.

It is important to note that a concentration of deformation into a more or less well-defined band does not necessarily constitute localization in the sense used here. We use the term localization to refer to situations in which the concentration of deformation into a band emerges as an outcome of the constitutive behavior of the material. Accordingly, the orientation of the band is characteristic of the material, rather than a consequence of boundary conditions. We will refer to such a band of localized deformation as a shear band, although in general dilatation as well as shear takes place within the band.

Since large strains accumulate inside a shear band without substantially affecting the strains in the surrounding material [8, 9], shear bands can only be accurately described by a

* M. Ortiz and Y. Leroy gratefully acknowledge support from the Office of Naval Research under grant N00014-85-K-0720. A. Needleman is grateful for the support provided by the U.S. National Science Foundation through grant MSM-8419338.

conventional displacement finite element method if the band interfaces follow element boundaries. Furthermore, the mesh sets the minimum band thickness at one element width. Thus, in order to accurately resolve a narrow shear band, small elements are required, with element boundaries that follow band directions. Finite element analyses of shear bands based on fine meshes of quadrilateral elements built up from four constant strain triangles have given sharply localized deformation modes, see e.g. [10, 11] and the review of Needleman and Tvergaard [12]. A material instability analysis [13–17] is used to orient the quadrilaterals. Localization is found in numerical calculations even when the mesh is not optimally designed, as discussed in [10], but with a certain delay and with some mesh-induced shear band broadening.

In a two-dimensional rectangular mesh, quadrilaterals built-up of four crossed triangles can resolve narrow bands of deformation in four directions; parallel with the sides of the quadrilateral and with the element diagonals. By way of contrast, isoparametric quadrilaterals can only resolve such narrow bands parallel with the element sides. Finite element analyses of oblique localized deformation bands using isoparametric quadrilateral elements, e.g. [18–20], do exhibit the tendency for shear bands to form when appropriate critical conditions are reached but have not exhibited the sharp localization obtained using crossed triangles.

However, the crossed triangle finite element formulation is specifically geared to two-dimensional problems and it does require careful mesh design to account for likely directions of localization. In this paper a method is proposed which aims at enhancing the performance of isoparametric elements in problems involving strain localization. The formulation here is restricted to small displacement gradient theory and to rate-independent constitutive relations. The method uses a material instability bifurcation analysis [13–17], carried out at the element level, to determine the geometry of the ensuing localized deformation modes. When the onset of localization is detected, the element interpolation is extended by adding to it suitably defined shape functions that reproduce the localized deformation modes. These additional shape functions render the element incompatible, but we show that the element satisfies the patch test [21, 22]. The extra degrees of freedom representing the amplitudes of the localized modes are eliminated by static condensation. It should be emphasized that all these operations can be implemented at the element level. The proposed methodology can be applied to two- and three-dimensional problems and does not require a mesh design to take explicit account of likely directions of localization. Pietruszcak and Mroz [23] previously incorporated a shear band mode of deformation into a finite element formulation. However, in their approach, the localized shear band is specified by the constitutive relation as the sole mode of inelastic deformation and the element strain rates are directly given in terms of conventional shape functions.

Numerical results are presented in Section 4 for localization in both nearly incompressible solids and in compressible solids. Even in the absence of shear bands, isoparametric elements are of limited value for nearly incompressible solids, such as the classical plastic solid. Mesh locking occurs as a result of the near incompressibility in the fully plastic range [24]. This difficulty can be overcome through the use of a method to handle internal constrains; for example, here we use a $\bar{\boldsymbol{B}}$ technique [25]. It bears emphasis, however, that to resolve localized deformation patterns in a nearly incompressible solid it is necessary, but not sufficient, to prevent mesh locking. Our numerical results show that the enhanced element introduced here does resolve localization more sharply than the underlying $\bar{\boldsymbol{B}}$-isoparametric element. Also, for

compressible solids, where mesh locking due to incompressibility is not an issue, numerical results are presented that illustrate the improved performance of the enhanced element.

2. Localization as a bifurcation phenomenon

In this section we review some aspects of the general theory of localization of inelastic deformations. Some of the basic principles underlying the theory follow from Hadamard's studies of elastic stability [13], extended to the inelastic context by Thomas [16], Hill [14], Mandel [15], and Rice [17]. Here, for simplicity, attention is confined to infinitesimal deformations and thermally decoupled, rate-independent material behavior.

Consider a homogeneous, homogeneously deformed solid subjected to quasi-static increments of deformation $\dot{\boldsymbol{\varepsilon}}$. We wish to determine if a *bifurcation* can occur in such a manner that subsequent deformations become discontinuous across a plane of orientation $\boldsymbol{n}$. Let $\boldsymbol{u}$ be the displacement field in the solid. Whereas $\boldsymbol{u}$ itself remains continuous after the onset of localization, the displacement gradients $\nabla \boldsymbol{u}$ will exhibit a jump across the plane of discontinuity, i.e.,

$$[\![u_{i,j}]\!] \equiv u^{+}_{i,j} - u^{-}_{i,j} \neq 0 , \tag{1}$$

where the superindex '+' refers to the plus side of the plane of discontinuity and '−' to the minus side. Maxwell's compatibility conditions necessitate that the jump (1) be of the form

$$[\![u_{i,j}]\!] = g_i n_j \tag{2}$$

for some vector $\boldsymbol{g}$. Let us further define $\boldsymbol{m}$ to be the unit vector along $\boldsymbol{g}$, i.e.,

$$m_i \equiv g_i / g , \qquad g \equiv |\boldsymbol{g}| . \tag{3}$$

The pair of unit vectors $\boldsymbol{m}$ and $\boldsymbol{n}$ entirely define the nature of the discontinuity. The corresponding strain jump is given by

$$[\![\varepsilon_{ij}]\!] = \tfrac{1}{2}(g_i n_j + g_j n_i) . \tag{4}$$

Often, two parallel planes of discontinuity pair up to form a band of intensely deformed material. Two limiting cases are noteworthy:

(a) $\boldsymbol{m}$ *orthogonal to* $\boldsymbol{n}$. The material in the band deforms in simple shear, i.e., a *shear band* develops.

(b) $\boldsymbol{m}$ *parallel to* $\boldsymbol{n}$. The band undergoes extension normal to the planes of discontinuity. In certain circumstances this can be interpreted as a *splitting* failure mode.

Shear bands are characteristic of materials exhibiting isochoric plasticity. On the other hand, splitting failure modes can be thought of as idealizations of the separation processes which occur during progressive brittle failure. In between these two extremes lies a continuous spectrum of mixed failure modes for which $\boldsymbol{m}$ and $\boldsymbol{n}$ are neither orthogonal nor parallel. Plastic-fracturing materials such as concrete, rocks, and ceramics are capable of failing in mixed modes, with the angle between $\boldsymbol{m}$ and $\boldsymbol{n}$ lying anywhere from 0° to 90° [17, 26, 27].

We next investigate under what conditions localized failure modes are possible. To this end, let us assume that the solid is at the onset of localization. At this point, the stresses $\boldsymbol{\sigma}$ and strains $\boldsymbol{\varepsilon}$ are continuous throughout the body. However, the stress and strain rates $\dot{\boldsymbol{\sigma}}$ and $\dot{\boldsymbol{\varepsilon}}$ will exhibit discontinuities across a plane whose orientation is to be determined. Assuming rate-independent material behavior the incremental stress-strain relations take the form

$$\dot{\sigma}_{ij} = D_{ijkl}\dot{\varepsilon}_{kl} , \tag{5}$$

where $\boldsymbol{D}$ is the tangent stiffness tensor for the material. Rate independence implies that $\boldsymbol{D}$ is homogeneous of degree zero in $\dot{\boldsymbol{\varepsilon}}$. We restrict attention to cases where $\boldsymbol{D}$ is piecewise independent of $\dot{\boldsymbol{\varepsilon}}$. For example, in classical plasticity $\boldsymbol{D}$ has two branches, one corresponding to plastic loading, the other to elastic unloading.

For elastic-plastic solids, the localization bifurcation analysis is carried out using the same branch of the moduli $\boldsymbol{D}$ across the incipient planes of discontinuity, which corresponds to investigating bifurcation for a *linear comparison solid* [33, 34]. Hence, taking jumps in (5) leads to

$$[\![\dot{\sigma}_{ij}]\!] = D_{ijkl}[\![\dot{\varepsilon}_{kl}]\!] . \tag{6}$$

Equilibrium across the discontinuity planes requires that the tractions $\boldsymbol{t}$ be continuous, i.e.,

$$[\![\dot{t}_j]\!] = [\![n_i\dot{\sigma}_{ij}]\!] = n_i[\![\dot{\sigma}_{ij}]\!] = 0 . \tag{7}$$

Combining (6) and (7), it follows that

$$n_i D_{ijkl}[\![\dot{\varepsilon}_{kl}]\!] = 0 . \tag{8}$$

Finally, using the kinematic relation (4) and the definition (3) we obtain

$$A_{jk}(\boldsymbol{n})m_k = (n_i D_{ijkl} n_l)m_k = 0 . \tag{9}$$

This condition has to be satisfied by $\boldsymbol{m}$ and $\boldsymbol{n}$ for the localized mode to be possible. The onset of localization occurs at the first point in the deformation history for which a nontrivial solution of (9) exists. For localization to occur along the direction $\boldsymbol{n}$, the localization matrix $\boldsymbol{A}(\boldsymbol{n})$ has to have at least one zero eigenvalue. This in turn necessitates

$$f(\boldsymbol{n}) \equiv \det(\boldsymbol{A}(\boldsymbol{n})) = 0 . \tag{10}$$

If a unit vector $\boldsymbol{n}$ satisfying (10) can be found, the corresponding vector $\boldsymbol{m}$ which completes the definition of the localized mode follows from (9).

A numerical procedure for computing $\boldsymbol{m}$ and $\boldsymbol{n}$ from the above equations is given in Appendix A. In two dimensions, the localization angles can be computed directly as the roots of a cubic polynomial, while in three dimensions the localization directions are computed iteratively. An example of application of the solution procedure to complex three-dimensional constitutive equations is found in [27].

3. An assumed strain finite element method for localized failure analysis

It has long been recognized [10] that isoparametric elements face inherent limitations in the presence of localized deformations. The essence of the problem can be illustrated by means of Fig. 1, which shows a shear band traversing a regular mesh at 45°. The elements on the boundary of the shear band should exhibit a strain discontinuity. However, such a deformation pattern is not well represented within the isoparametric interpolation. On the contrary, the element tries to conform to the deformation field by averaging the deformation on both sides of the discontinuity. As a result, the true discontinuous behavior may be smeared out over several elements or in some cases precluded altogether.

A numerical procedure which circumvents these difficulties is proposed next. For simplicity, attention is confined to infinitesimal deformations. The method can be described as follows:

(i) For every element in the mesh a localization analysis of the type described in Section 2 is carried out at the reduced quadrature points, where the stresses and other state variables are computed most accurately [35]. For instance, in 4-node and 9-node isoparametric elements localization is investigated at the centroid and the 2×2 Gauss points, respectively. This analysis is repeated at every step of the solution process until the onset of localization is detected at one or more reduced quadrature points.

(ii) From this point on, suitable deformation modes which exactly reproduce the discontinuous deformation patterns are added to the element or elements where localization is detected. The extra degrees of freedom are eliminated at the element level by means of static condensation.

This approach takes advantage of the fact that considerable information concerning the localization process can be readily obtained at the element level. The method aims at utilizing this information to enhance the performance of the element in the presence of localized failure.

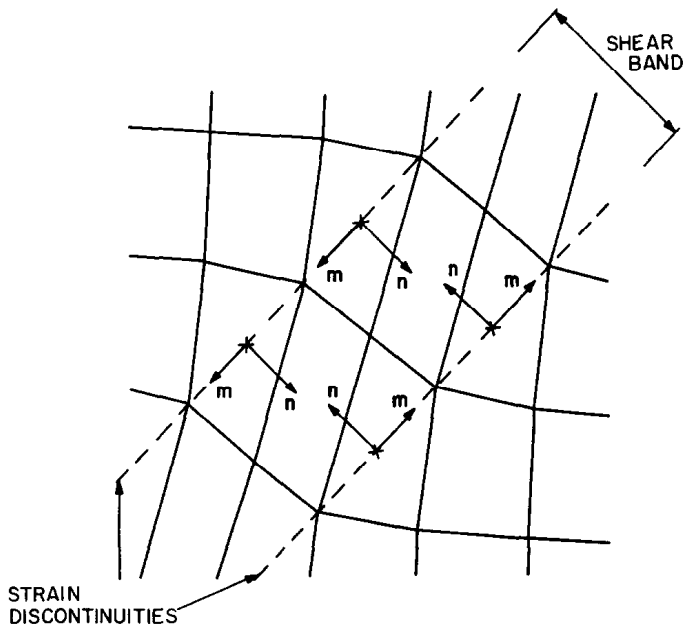

Fig. 1. Close-up view of the central portion of the shear band shown in Fig. 17.

3.1. Localized deformation modes

We envision a generic element in which the displacement field is interpolated as

$$u_i(\boldsymbol{x}) = \sum_{a=1}^{N} u_{ia} N_a(\boldsymbol{x}) , \tag{11}$$

where u_{ia} are the nodal displacements, $N_a(\boldsymbol{x})$ are the interpolation functions, and the sum extends to all N nodes in the element. A typical example is given by the serendipity family of 4- to 9-node isoparametric elements. Let us further denote by $\{\xi_{ir}, r = 1, \ldots, \mathrm{NQ}\}$ the coordinates of the reduced quadrature points. Here the subindex r ranges over all NQ reduced quadrature points in the element.

Based on the state variables computed at the points $\boldsymbol{\xi}_r$ a localization analysis of the type described in Section 2 can be carried throughout the solution process. Let us assume that in the generic element under consideration and at some stage of the solution several bifurcations have been detected resulting in NL localized modes. The geometry of these deformation modes is fully determined by pairs of unit vectors $\{(m_{i\alpha}, n_{i\alpha}), \alpha = 1, \ldots, \mathrm{NL}\}$ representing the displacement direction and the normal to the surface of discontinuity, respectively. Furthermore, let $\boldsymbol{\xi}_\alpha$ denote the reduced quadrature point at which the αth localized mode has been detected.

Localized deformation modes exhibit a strain discontinuity along the surface of normal $\boldsymbol{n}_\alpha$ passing through $\boldsymbol{\xi}_\alpha$. In order to accommodate these deformation modes, we extend the element interpolation by means of suitably defined shape functions which closely reproduce the localized deformation patterns. To this end, for each localized mode we define the functions

$$M^+_{i\alpha}(\boldsymbol{x}) = \begin{cases} m_{i\alpha}[\boldsymbol{n}_\alpha \cdot (\boldsymbol{x} - \boldsymbol{\xi}_\alpha)] , & \text{if } \boldsymbol{n}_\alpha \cdot (\boldsymbol{x} - \boldsymbol{\xi}_\alpha) \geqslant 0 , \\ 0 , & \text{otherwise} , \end{cases} \tag{12}$$

$$M^-_{i\alpha}(\boldsymbol{x}) = \begin{cases} -m_{i\alpha}[\boldsymbol{n}_\alpha \cdot (\boldsymbol{x} - \boldsymbol{\xi}_\alpha)] , & \text{if } \boldsymbol{n}_\alpha \cdot (\boldsymbol{x} - \boldsymbol{\xi}_\alpha) \leqslant 0 , \\ 0 , & \text{otherwise} , \end{cases} \tag{13}$$

where no sum is implied on the index α. These functions exhibit a jump across the surface of discontinuity

$$[\![(M^+_{i\alpha})_{,j}]\!] = [\![(M^-_{i\alpha})_{,j}]\!] = m_{i\alpha} n_{j\alpha} . \tag{14}$$

Consequently, any convex combination

$$M_{i\alpha}(\boldsymbol{x}) = (1 - \lambda_\alpha) M^-_{i\alpha}(\boldsymbol{x}) + \lambda_\alpha M^+_{i\alpha}(\boldsymbol{x}) \tag{15}$$

of $M^+_{i\alpha}$ and $M^-_{i\alpha}$ exhibits the same jump (14). Thus, (15) defines a one-parameter family of possible shape functions for the localized modes. Adding these shape functions to the element interpolation, the local displacement field becomes

$$u_i(\boldsymbol{x}) = \sum_{a=1}^{N} u_{ia} N_a(\boldsymbol{x}) + \sum_{\alpha=1}^{\mathrm{NL}} \gamma_\alpha M_{i\alpha}(\boldsymbol{x}) , \tag{16}$$

where $\{\gamma_\alpha, \alpha = 1, \ldots, \mathrm{NL}\}$ are the amplitudes of the localized modes. It should be noted that shape functions (15) are *incompatible*, i.e., in general do not satisfy the C^0 continuity requirement across the element boundary and the element becomes *nonconforming*.

The element strain field is computed from (16) to be

$$\begin{aligned}\varepsilon_{ij}(\boldsymbol{x}) &= \tfrac{1}{2}(u_{i,j}(\boldsymbol{x}) + u_{j,i}(\boldsymbol{x})) \\ &= \sum_{a=1}^{N} \tfrac{1}{2}(u_{ia}N_{a,j}(\boldsymbol{x}) + u_{ja}N_{a,i}(\boldsymbol{x})) + \sum_{\alpha=1}^{\mathrm{NL}} \tfrac{1}{2}\gamma_\alpha((M_{i\alpha})_{,j}(\boldsymbol{x}) + (M_{j\alpha})_{,i}(\boldsymbol{x}))\,. \end{aligned} \tag{17}$$

For subsequent derivations it proves convenient to recast this expression in matrix form. Let $\boldsymbol{u}_1$ denote the nodal displacement array and $\boldsymbol{u}_2$ the collection of amplitudes γ_α of the additional incompatible modes. Then (17) can be expressed in the more compact form

$$\boldsymbol{\varepsilon}(\boldsymbol{x}) = \boldsymbol{B}_1\boldsymbol{u}_1 + \boldsymbol{B}_2\boldsymbol{u}_2\,. \tag{18}$$

It follows from (12) and (15) that the compatibility matrix $\boldsymbol{B}_2$ takes the form

$$(\boldsymbol{B}_2)_{ij\alpha} = \begin{cases} \tfrac{1}{2}\lambda_\alpha(m_{i\alpha}n_{j\alpha} + m_{j\alpha}n_{i\alpha}) & \text{if } \boldsymbol{n}_\alpha\cdot(\boldsymbol{x} - \boldsymbol{\xi}_\alpha) > 0\,, \\ -\tfrac{1}{2}(1-\lambda_\alpha)(m_{i\alpha}n_{j\alpha} + m_{j\alpha}n_{i\alpha})\,, & \text{if } \boldsymbol{n}_\alpha\cdot(\boldsymbol{x} - \boldsymbol{\xi}_\alpha) < 0\,, \end{cases} \tag{19}$$

so that the element strain field exhibits a jump

$$[\![\varepsilon_{ij}(\boldsymbol{x})]\!] = \tfrac{1}{2}\gamma_\alpha(m_{i\alpha}n_{j\alpha} + m_{j\alpha}n_{i\alpha}) \tag{20}$$

across the αth surface of discontinuity. Thus, the parameters γ_α represent the magnitude of the strain discontinuity associated with the αth localized mode.

It is implied in (18) that in the absence of localized modes the element strain field takes the form $\boldsymbol{\varepsilon}(\boldsymbol{x}) = \boldsymbol{B}_1(\boldsymbol{x})\boldsymbol{u}_1$, where $\boldsymbol{B}_1$ results from applying the strain-displacement relations to the conforming interpolation (11). It was noted in [24] that in applications involving isochoric perfect plasticity this formulation results in an overly stiff response due to the poor handling by the element of the near-incompressibility which accompanies extensive plastic flow. A number of techniques have been proposed to alleviate the locking phenomena associated with internal constraints such as incompressibility. In this work we adopt Hughes' $\bar{\boldsymbol{B}}$ method [25] which for the 4-node quadrilateral consists of replacing the compatibility matrix $\boldsymbol{B}_1$ by a modified $\bar{\boldsymbol{B}}_1$ of the form

$$\bar{\boldsymbol{B}}_1(\boldsymbol{x}) \equiv \boldsymbol{B}_1^{\mathrm{dev}}(\boldsymbol{x}) + \varepsilon\boldsymbol{B}_1^{\mathrm{vol}}(\boldsymbol{x}) + (1-\varepsilon)\boldsymbol{B}_1^{\mathrm{vol}}(\boldsymbol{x}_0)\,. \tag{21}$$

Here, $\boldsymbol{B}_1^{\mathrm{dev}}$ and $\boldsymbol{B}_1^{\mathrm{vol}}$ are defined so as to give the deviatoric and volumetric parts of the strain tensor when multiplied by $\boldsymbol{u}_1$, $\boldsymbol{x}_0$ is the centroid of the element, and ε is a small stabilization parameter which is included to suppress spurious pressure modes [28]. For the 9-node element, $\boldsymbol{B}_1^{\mathrm{vol}}$ is computed at the reduced quadrature points and extrapolated to the rest of the element by means of suitable shape functions. Hughes' $\bar{\boldsymbol{B}}$ method is closely related to selective reduced integration techniques and to mixed methods, see e.g. the review of Hughes et al. [29].

Substituting $\boldsymbol{B}_1$ in (18) by the modified compatibility matrix $\bar{\boldsymbol{B}}_1$ the element strain field finally takes the form

$$\boldsymbol{\varepsilon}(\boldsymbol{x}) = \bar{\boldsymbol{B}}_1 \boldsymbol{u}_1 + \boldsymbol{B}_2 \boldsymbol{u}_2 \,. \tag{22}$$

Let us define the stiffness submatrices

$$\boldsymbol{K}_{11} = \int_{\Omega^e} \bar{\boldsymbol{B}}_1^{\mathrm{t}} \boldsymbol{D} \bar{\boldsymbol{B}}_1 \, \mathrm{d}V \,, \qquad \boldsymbol{K}_{12} = \boldsymbol{K}_{21}^{\mathrm{t}} = \int_{\Omega^e} \bar{\boldsymbol{B}}_1^{\mathrm{t}} \boldsymbol{D} \boldsymbol{B}_2 \, \mathrm{d}V \,, \qquad \boldsymbol{K}_{22} = \int_{\Omega^e} \boldsymbol{B}_2^{\mathrm{t}} \boldsymbol{D} \boldsymbol{B}_2 \, \mathrm{d}V \,, \tag{23}$$

where Ω^e signifies the domain of the element and $\boldsymbol{D}$ is the tangent stiffness tensor of the material. Since the localized modes represent internal degrees of freedom of the element, the corresponding amplitudes $\boldsymbol{u}_2$ can be eliminated by static condensation [30] to obtain

$$\dot{\boldsymbol{u}}_2 = -\boldsymbol{K}_{22}^{-1} \boldsymbol{K}_{21} \dot{\boldsymbol{u}}_1 \,, \tag{24}$$

and the effective element stiffness becomes

$$\boldsymbol{K} = \boldsymbol{K}_{11} - \boldsymbol{K}_{12} \boldsymbol{K}_{22}^{-1} \boldsymbol{K}_{21} \,. \tag{25}$$

It should be emphasized that all the matrix operations indicated in (25) can be carried out at the element level.

As can be seen from (25), in the present method the stiffness matrix $\boldsymbol{K}_{11}$ of the underlying conforming element is modified by means of a term which represents the net effect of the added localized modes. In Section 4 it is shown by way of numerical examples that the enhanced element is more conducive to localization and provides sharper results than those obtained from the $\bar{\boldsymbol{B}}$ method alone.

3.2. Patch test

In Section 3.1 it was noted that the introduction of localized deformation modes renders the element nonconforming. To insure that the convergence properties of the underlying conforming element are not altered, the incompatible modes have to be defined in such a way that the patch test is satisfied. This test determines whether or not the element consistently reproduces states of constant strain. If so, convergence takes place within each element, e.g. [28].

The definition of shape functions (15) contains a set of free, as yet undetermined parameters λ_α. Next, it is shown that the value of these parameters can be uniquely determined from the requirement that the element satisfy the patch test. Taylor et al. [22] derived a necessary condition for the patch test to be passed by a nonconforming element. With the present notation such a condition reads

$$\int_{\Omega^e} \boldsymbol{B}_2 \, \mathrm{d}V = \boldsymbol{0} \,. \tag{26}$$

In view of (19), (26) necessitates

$$\tfrac{1}{2}[-(1-\lambda_\alpha)A_\alpha^{e-} + \lambda_\alpha A_\alpha^{e+}](m_{i\alpha}n_{j\alpha} + m_{j\alpha}n_{i\alpha}) = 0\,, \tag{27}$$

where A_α^{e+} and A_α^{e-} are the areas of the element subdomains lying on the plus and the minus sides of the αth surface of discontinuity, respectively. Condition (27) is satisfied by setting

$$-(1-\lambda_\alpha)A_\alpha^{e-} + \lambda_\alpha A_\alpha^{e+} = 0\,, \tag{28}$$

which yields

$$\lambda_\alpha = A_\alpha^{e-}/A^e\,, \tag{29}$$

where $A^e = A_\alpha^{e+} + A_\alpha^{e-}$ is the total area of the element. In practice, satisfactory results are obtained by computing the areas A_α^{e+} and A_α^{e-} by numerical integration.

3.3. Formulation as an assumed strain method

A broad class of finite element schemes commonly referred to as $\bar{\boldsymbol{B}}$ methods consists of postulating a relation $\boldsymbol{\varepsilon} = \bar{\boldsymbol{B}}\boldsymbol{u}$ for some suitably defined operator $\bar{\boldsymbol{B}}$ and a tangent stiffness matrix of the form

$$\boldsymbol{K} = \int_{\Omega^e} \bar{\boldsymbol{B}}^{\mathrm{t}}\boldsymbol{D}\bar{\boldsymbol{B}}\,\mathrm{d}V\,. \tag{30}$$

This class of methods originated with the pioneering paper of Hughes [25] and has been particularly successful in overcoming mesh locking difficulties associated with internal constraints. The formulation proposed here can be rephrased as a $\bar{\boldsymbol{B}}$ method by noting that (25) can be alternatively expressed as

$$\boldsymbol{K} = \int_{\Omega^e} (\bar{\boldsymbol{B}}_1 - \boldsymbol{B}_2\boldsymbol{K}_{22}^{-1}\boldsymbol{K}_{21})^{\mathrm{t}}\boldsymbol{D}(\bar{\boldsymbol{B}}_1 - \boldsymbol{K}_{12}\boldsymbol{K}_{22}^{-1}\boldsymbol{B}_2)\,\mathrm{d}V\,. \tag{31}$$

Comparison of (30) and (31) warrants the identification

$$\bar{\boldsymbol{B}} \equiv \bar{\boldsymbol{B}}_1 - \boldsymbol{B}_2\boldsymbol{K}_{22}^{-1}\boldsymbol{K}_{21}\,. \tag{32}$$

Thus, the proposed formulation can be regarded as a $\bar{\boldsymbol{B}}$ method in which the compatibility operator is postulated to take the form (32).

The expression (31) for the effective stiffness matrix can be directly obtained from the Hellinger–Reissner variational principle. This principle characterizes the equilibrium and compatibility equations as the Euler equations of the potential

$$L(\dot{\boldsymbol{u}}, \dot{\boldsymbol{\varepsilon}}) = \int_\Omega [\tfrac{1}{2}D_{ijkl}\dot{\varepsilon}_{ij}(\dot{u}_{k,l} + \dot{u}_{l,k}) - \tfrac{1}{2}D_{ijkl}\dot{\varepsilon}_{ij}\dot{\varepsilon}_{kl} - \dot{f}_i\dot{u}_i]\,\mathrm{d}V - \int_{\partial\Omega_\tau} \dot{t}_i\dot{u}_i\,\mathrm{d}S\,, \tag{33}$$

where Ω is the domain occupied by the body, $\partial\Omega_\tau$ is the traction boundary, and $\boldsymbol{f}$ and $\boldsymbol{t}$ denote the body forces and applied tractions, respectively. Guided by the results obtained from the

static condensation procedure we postulate the following two-field interpolation for displacements and strains:

$$u_i(\boldsymbol{x}) = \sum_{a=1}^{N} u_{ia} N_a(\boldsymbol{x}) , \qquad \dot{\boldsymbol{\varepsilon}}(\boldsymbol{x}) = \bar{\boldsymbol{B}}\dot{\boldsymbol{u}}_1 = (\bar{\boldsymbol{B}}_1 - \boldsymbol{B}_2 \boldsymbol{K}_{22}^{-1} \boldsymbol{K}_{21}) \dot{\boldsymbol{u}}_1 , \tag{34}$$

where, as before, $\boldsymbol{u}_1$ denotes the collection of nodal displacements u_{ia} and N_a are the conformal shape functions. Substituting the interpolated fields (34) into the Hellinger–Reissner potential the discretized Euler equations are found to be

$$\sum_e \left[\int_{\Omega^e} \boldsymbol{B}_1^{\mathrm{t}} \boldsymbol{D} \bar{\boldsymbol{B}} \, \mathrm{d}V \right] \dot{\boldsymbol{u}}_1 = \sum_e \dot{\boldsymbol{f}}_1 , \tag{35a}$$

$$\left[\int_{\Omega^e} \bar{\boldsymbol{B}}^{\mathrm{t}} \boldsymbol{D} (\boldsymbol{B}_1 - \bar{\boldsymbol{B}}) \, \mathrm{d}V \right] \dot{\boldsymbol{u}}_1 = \boldsymbol{0} , \tag{35b}$$

where the element forces are given by

$$(\boldsymbol{f}_1)_{ia} = \int_{\Omega^e} f_i N_a \, \mathrm{d}V + \int_{\partial\Omega_\tau^e} t_i N_a \, \mathrm{d}S . \tag{36}$$

It is interesting to note that only the conformal shape functions are involved in the computation of the element forces. It follows from (35a) that the element stiffness matrix takes the form

$$\boldsymbol{K} = \int_{\Omega^e} \boldsymbol{B}_1^{\mathrm{t}} \boldsymbol{D} \bar{\boldsymbol{B}} \, \mathrm{d}V . \tag{37}$$

On the other hand, satisfaction of (35b) for arbitrary incremental displacements necessitates

$$\int_{\Omega^e} \bar{\boldsymbol{B}}^{\mathrm{t}} \boldsymbol{D} (\boldsymbol{B}_1 - \bar{\boldsymbol{B}}) \, \mathrm{d}V = \boldsymbol{0} . \tag{38}$$

If this condition is identically satisfied the stiffness matrix (37) can be alternatively expressed in $\bar{\boldsymbol{B}}$ form,

$$\boldsymbol{K} = \int_{\Omega^e} \bar{\boldsymbol{B}}^{\mathrm{t}} \boldsymbol{D} \bar{\boldsymbol{B}} \, \mathrm{d}V . \tag{39}$$

A simple computation reveals that for the present choice of matrix $\bar{\boldsymbol{B}}$ (32), condition (38) is indeed identically satisfied. Hence the method can be directly derived from the Hellinger–Reissner variational principle. The conditions under which a $\bar{\boldsymbol{B}}$ method is variationally consistent were first elucidated in [31], where orthogonality conditions (38) were derived within the more general context of the Hu–Washizu principle.

Satisfaction of orthogonality conditions (38) not only places the method on a solid variational foundation but also has a consequence of some practical importance. Equation (35a) indicates that the internal forces evolve at a rate,

$$\dot{f}_1^{\text{int}} = \sum_e \left[\int_{\Omega^e} \boldsymbol{B}_1^{\text{t}} \boldsymbol{D} \bar{\boldsymbol{B}} \, \mathrm{d}V \right] \dot{\boldsymbol{u}}_1 \,. \tag{40}$$

Integrating in time we obtain the expression

$$f_1^{\text{int}} = \sum_e \int_{\Omega^e} \boldsymbol{B}_1^{\text{t}} \boldsymbol{\sigma} \, \mathrm{d}V \,. \tag{41}$$

Thus, the internal forces can be computed by using the conformal compatibility matrix $\boldsymbol{B}_1$ regardless of whether localized deformation modes have been added to the interpolation. On one hand, this has the effect of eliminating the overhead involved in computing the enhanced $\bar{\boldsymbol{B}}$ matrix during the computation of the internal forces. Secondly, (41) guarantees that as long as the stress history is continuous in time the internal forces will also be a continuous function of time. In particular, no sudden jumps will be experienced by the internal forces on adding a localized mode to the interpolation.

4. Numerical examples

In the course of conducting numerical tests, it was found that the performance of the element could be improved further by incorporating the incompatible modes as soon as the centroid plastifies. In general, the bifurcation condition (10) is not satisfied at that point. However, the vectors $\boldsymbol{n}$ and $\boldsymbol{m}$ can be computed as the minima of $\det(\boldsymbol{A}(\boldsymbol{n}))$ and as the minimum eigenvector of the resulting $\boldsymbol{A}(\boldsymbol{n})$, respectively. Under these conditions, the vectors $\boldsymbol{m}$ and $\boldsymbol{n}$ no longer are localization directions but can be thought of as defining the general trend towards localization. This extension of the method was used throughout the examples discussed next.

Considerable insight into the performance of the method can be obtained by examining the behavior of a single element. A first simple example of this nature is shown in Fig. 2. The

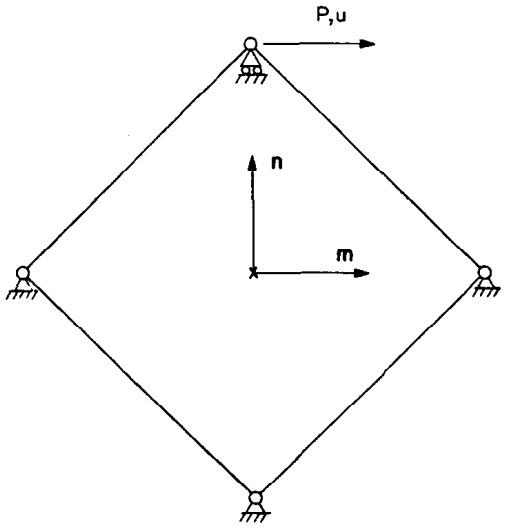

Fig. 2. Single-element test problem.

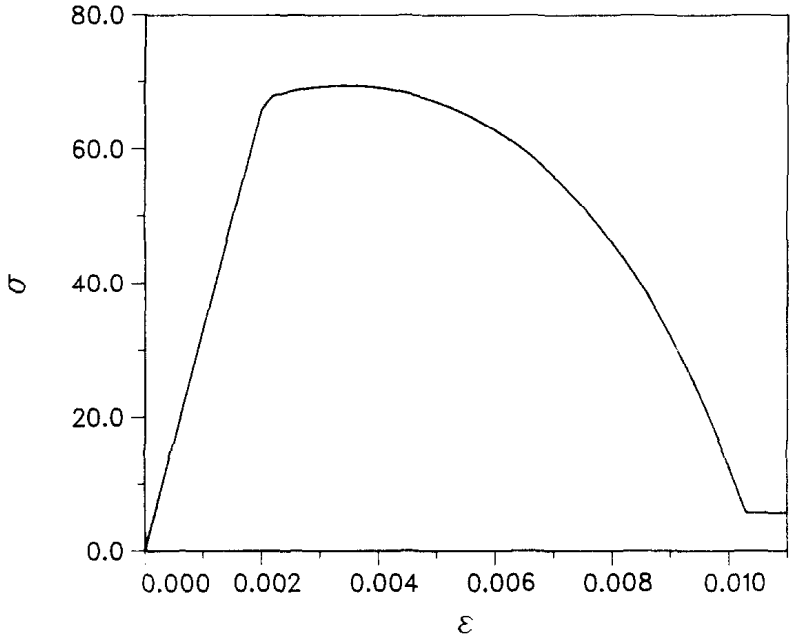

Fig. 3. Plane strain, uniaxial stress-strain curve used in single-element example.

problem concerns one element in which three nodes are constrained in both directions while displacements are prescribed on the fourth node which result in nonuniform shear across the element. The material is assumed to obey J_2-flow theory with a parabolically softening stress-strain law, Fig. 3, and plane strain conditions are enforced. The material constants used in the computations are: $E = 30\,000$, $\nu = 0.3$, $\sigma_y = 60$, $h_0 = 1000$, $\kappa = -10^6$, and $\sigma_c = 2$, where E and ν are the Young's modulus and Poisson's ratio, h_0 is the initial plastic modulus, κ is the

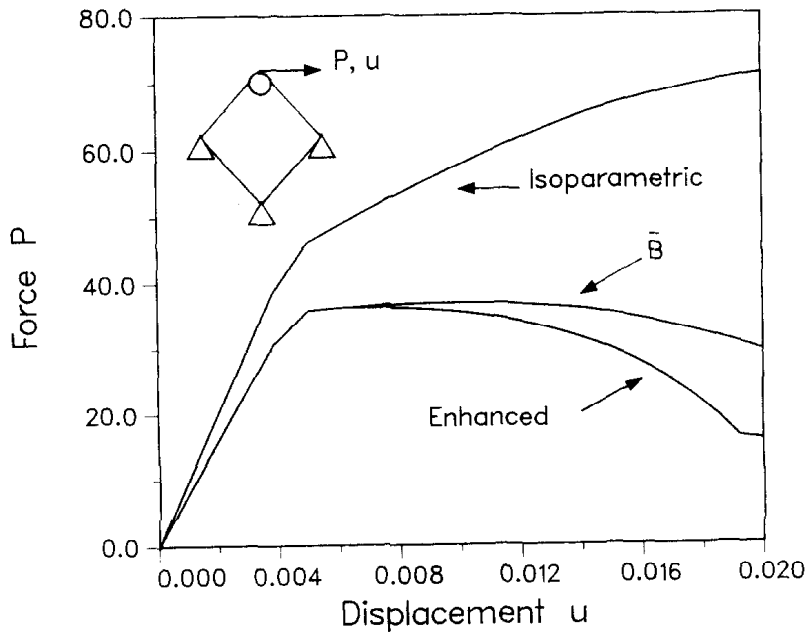

Fig. 4. Force-displacement curves for the single-element example.

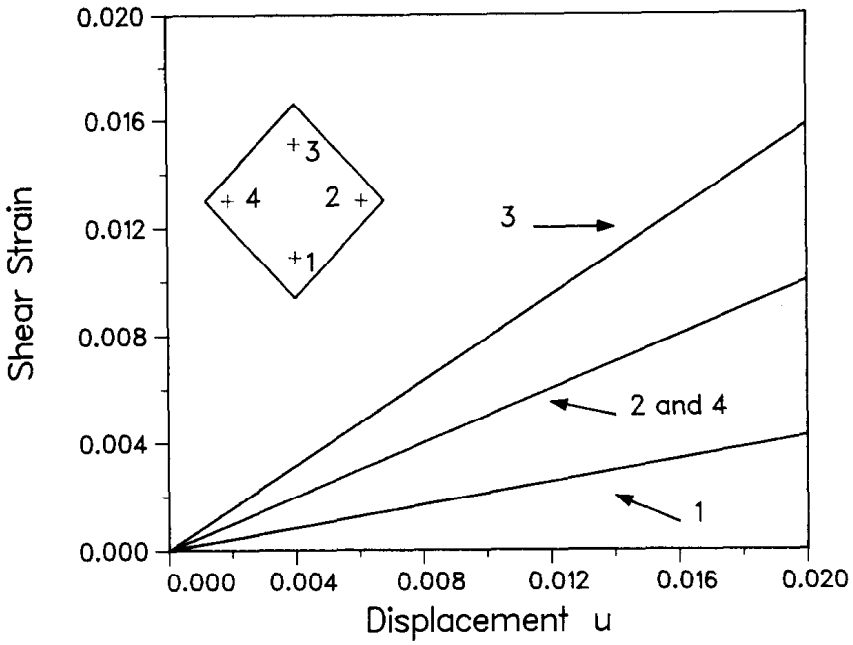

Fig. 5(a). Evolution of shear strains at Gauss quadrature points for the single-element example, $\bar{B}$ method.

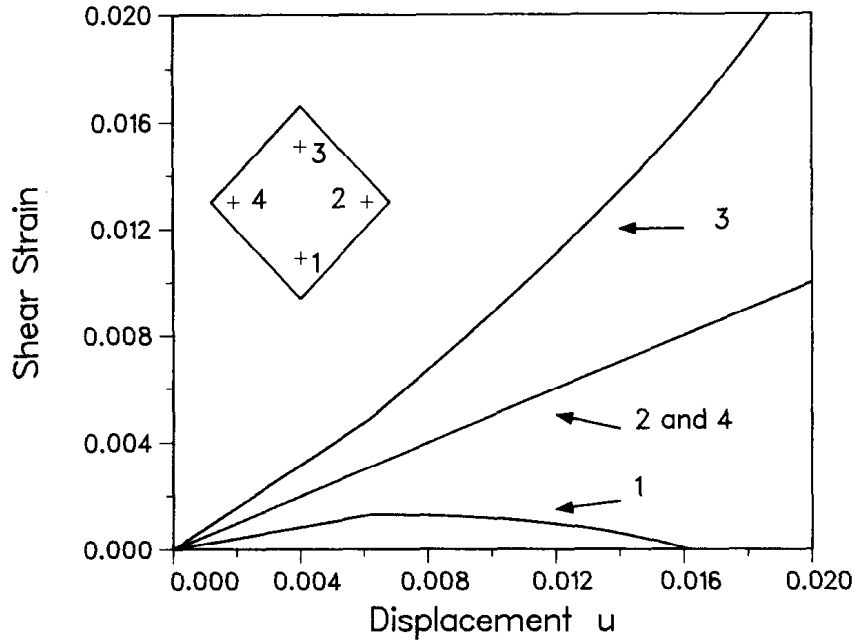

Fig. 5(b). Evolution of shear strains at Gauss quadrature points for the single-element example, enhanced element.

curvature of the stress-strain curve, and σ_c is a cut-off stress which is introduced to prevent the yield stress from vanishing. The computed force-displacement diagrams corresponding to an isoparametric element, Hughes' $\bar{B}$ method [25], and the present approach are shown in Fig. 4. Whereas the isoparametric element exhibits considerable residual stiffness once the element is fully plastified, both the $\bar{B}$ method and the enhanced element predict limit loads of similar magnitudes. However, the $\bar{B}$ method is seen to significantly retard the softening portion of the

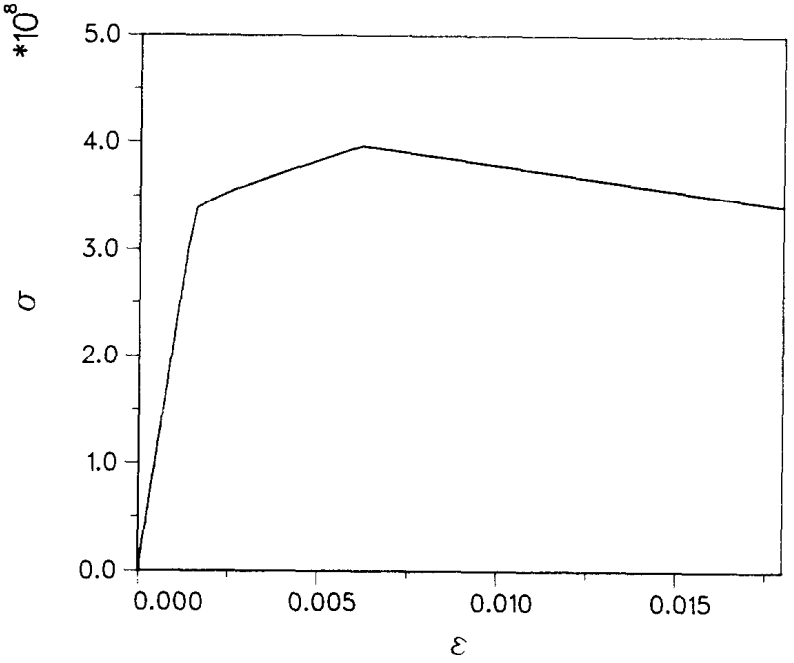

Fig. 6. Plane strain, uniaxial stress-strain curve used in examples shown in Figs. 7–21.

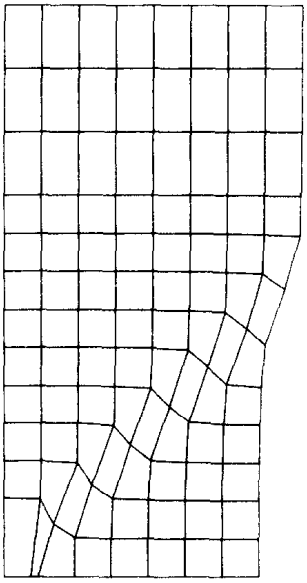

Fig. 7. Deformed mesh, displacements scaled by a factor of 10.

force-displacement curve with respect to the enhanced element. Furthermore, the nature of the failure mechanisms predicted by both methods is significantly different. Fig. 5 shows the computed strain histories at all quadrature points. It is seen that those obtained from the $\bar{\boldsymbol{B}}$ method show proportional growth and no tendency towards localization. By contrast, in the enhanced element a bifurcation is detected at the centroid which results in the localized mode shown in Fig. 2. From this point on, the strain within the lower half of the element steadily

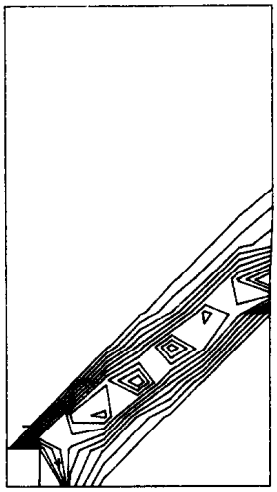

Fig. 8. Contours of effective plastic strain as computed from the enhanced element. The contour levels range from 0.64% to 6.4% in 10 equal intervals.

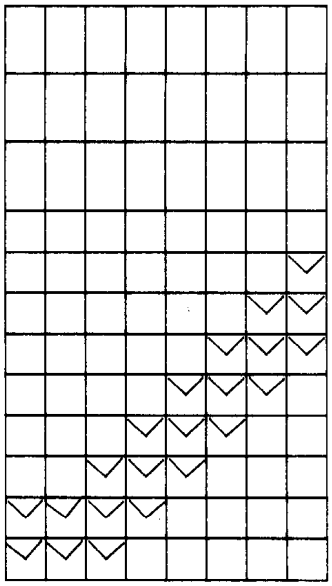

Fig. 9. Bifurcated elements and bifurcation directions.

decreases and all subsequent deformations are localized to the upper half. Thus, whereas adequate handling of incompressibility suffices to capture limit loads accurately it appears that to obtain sharp predictions of localized failure further structure needs to be added to the element.

The next set of examples is concerned with a material obeying J_2-flow theory and a trilinear stress-strain law with a downsloping branch, Fig. 6. The material constants utilized in all three

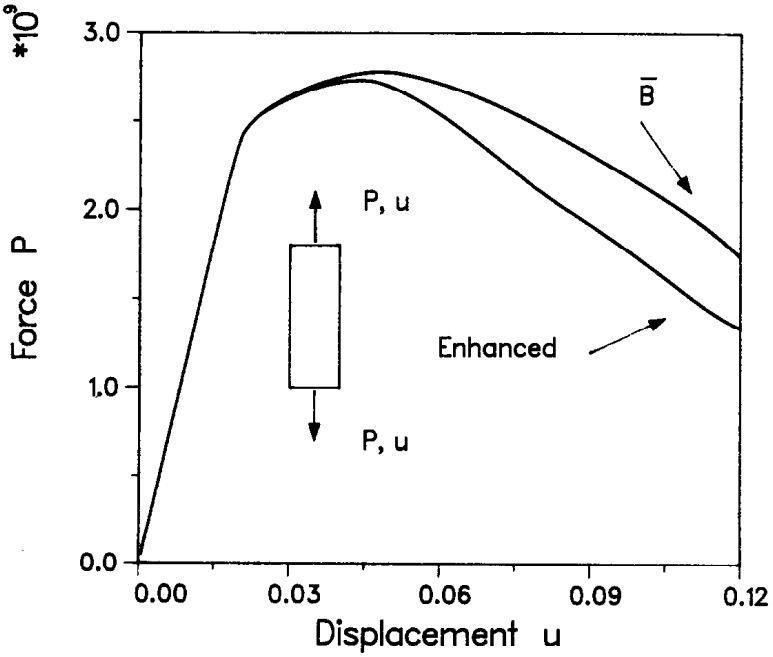

Fig. 10. Force-displacement curves.

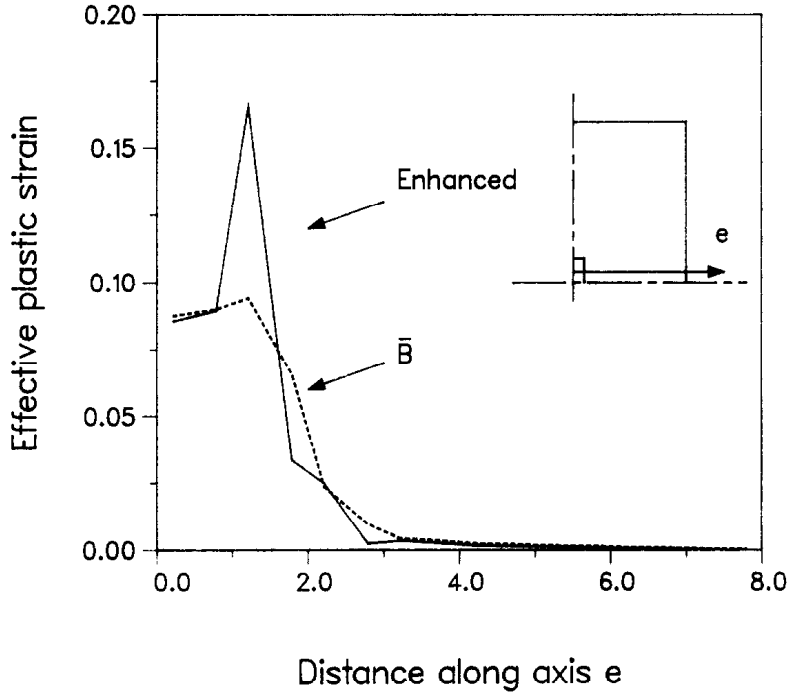

Fig. 11. Distribution of effective plastic strain across the shear band.

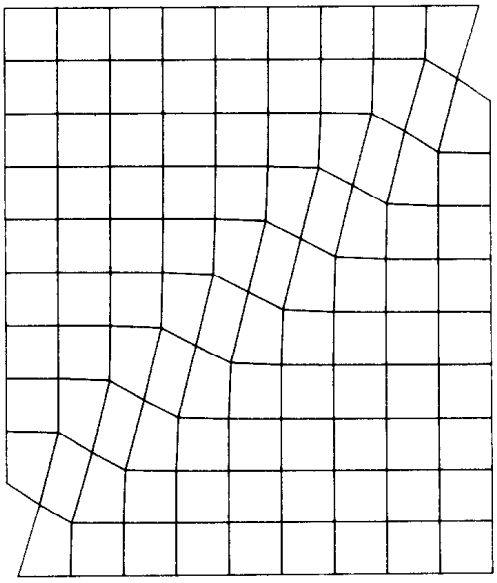

Fig. 12. Deformed mesh, displacements scaled by a factor of 10.

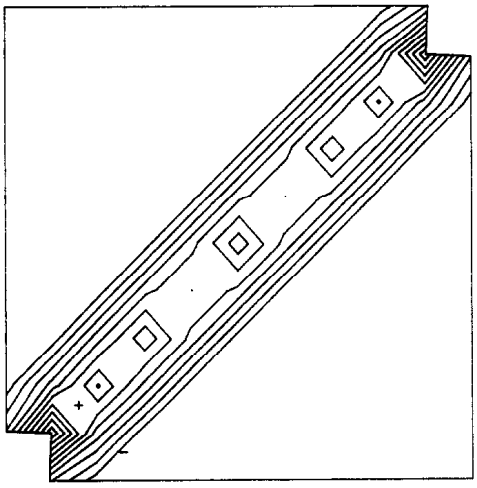

Fig. 13. Contours of effective plastic strain as computed from the enhanced element. The contour levels range from 0.52% to 6.2% in 10 equal intervals.

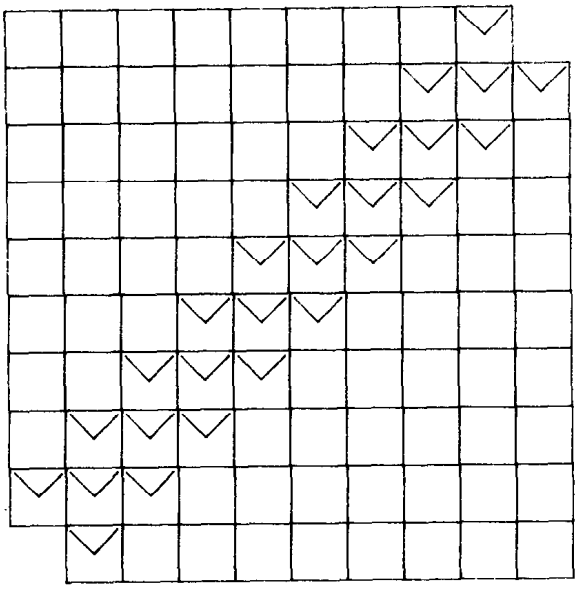

Fig. 14. Bifurcated elements and bifurcation directions.

examples are: $E = 2 \times 10^{11}$, $\nu = 0.3$, $h_0 = 5 \times 10^9$, with the same notation as above. At an effective plastic strain of 0.5%, the plastic modulus is changed to $h = -2 \times 10^9$. Finally, the stress-strain curve is cut off at a level $\sigma_c = 1000$. Plane strain conditions are assumed throughout.

The first example consists of a rectangular bar with an inhomogeneity at the center. The bar is subjected to prescribed uniform displacements at both ends which in the absence of the

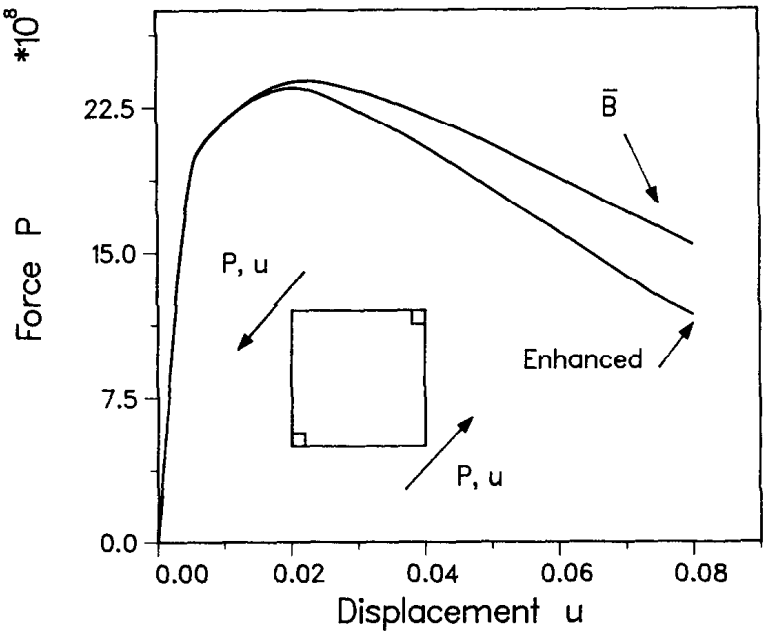

Fig. 15. Force-displacement curves.

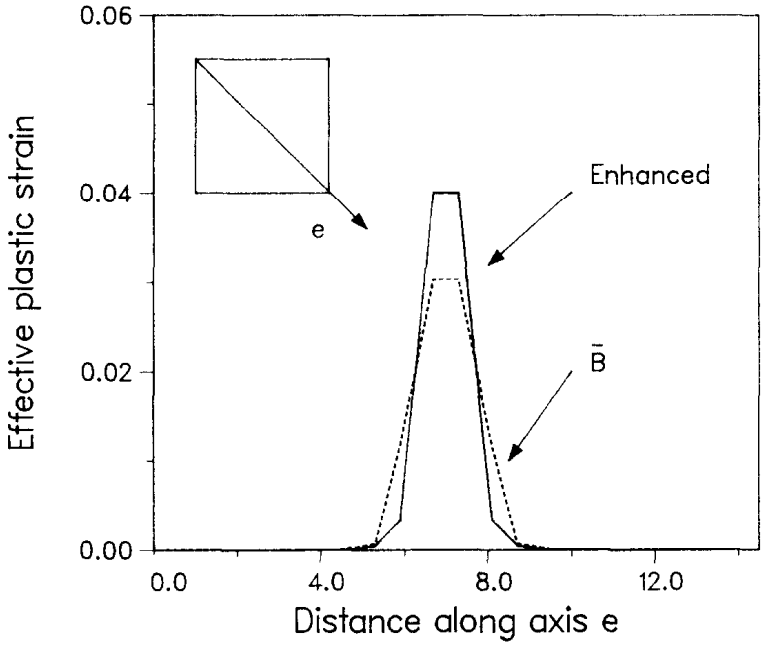

Fig. 16. Distribution of effective plastic strain across the shear band.

imperfection would result in a state of uniform stretch. The yield stress of the material is taken to be $\sigma_y = 3 \times 10^8$. The inhomogeneity is modeled as a weak element with all moduli reduced by a factor of 100 and the yield stress set to $\sigma_y = 10^6$. The effect of this imperfection is to nucleate a shear band which grows a 45° into the side of the specimen, Fig. 7. Level contours of effective plastic strain and the bifurcated elements are shown in Figs. 8 and 9. A well-developed shear band one element wide is clearly apparent.

A second example is concerned with shear band formation in a solid with a periodic array of inhomogeneities. The body is subjected to remote loads which in the absence of the inhomogeneities would result in a uniform shear deformation. The inhomogeneities are modelled as missing elements and act as nucleation sites from where shear bands emanate. The initial yield stress used in the computations is $\sigma_y = 2 \times 10^8$. Fig. 12 shows the deformed mesh corresponding to a prescribed overall shear deformation $\bar{\gamma} = 1.6\%$ and Fig. 13 depicts

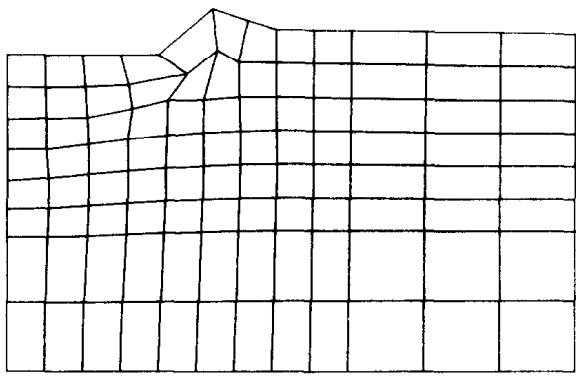

Fig. 17. Deformed mesh, displacements scaled by a factor of 5.

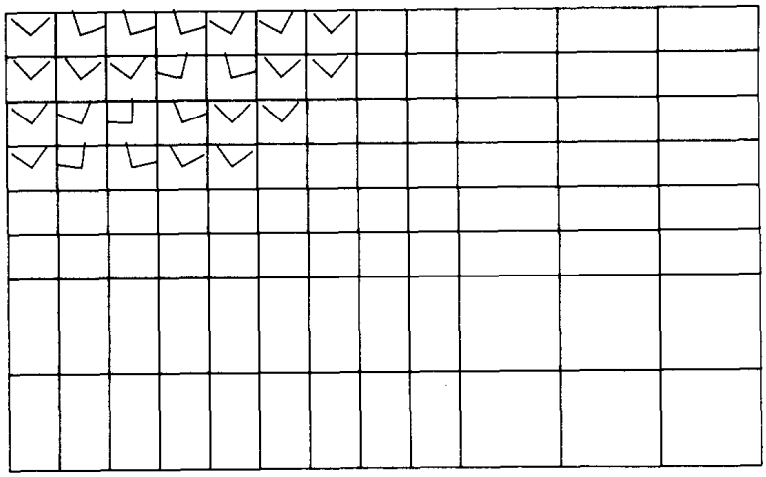

Fig. 18. Bifurcated elements and bifurcation directions.

the corresponding level contours of effective plastic strain. The results clearly exhibit a shear band spanning the inhomogeneities. The bifurcated elements and localization directions are shown in Fig. 14. It is seen that localization is confined to a diagonal band one element wide.

The third example is concerned with a rigid punch on a rectangular domain. In this case, following localization all plastic flow becomes confined to a circular band of material centered at the corner of the indentor, Fig. 17. This is in contrast to the situation found for stable and perfectly plastic materials, where a more diffuse deformation pattern is observed. This example aims at assessing the ability of the method to deal effectively with localization directions cutting across the mesh lines at arbitrary angles. The bifurcation directions shown in Fig. 18 appear to be determined by the nature of the flow and not to be influenced by the mesh geometry. A plot of the level contours of effective plastic strain is given in Fig. 19.

Figs. 10, 15, and 20 show the force-displacement curves computed for the aforementioned examples. In all cases it is observed that the $\bar{\boldsymbol{B}}$ method results in a significantly stiffer response in the softening range than the enhanced element. This conclusion is reinforced by the results shown in Figs. 11, 16, and 21, which show the distribution of effective plastic strains along selected cuts through the solids. Here, it is observed that the enhanced element results in levels of effective plastic strain 30 to 60% higher than those computed from the $\bar{\boldsymbol{B}}$ method. In cases where a shear band develops, the thickness of the shear band is consistently smaller for

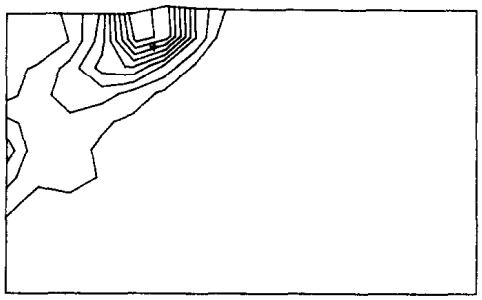

Fig. 19. Contours of effective plastic strain as computed from the enhanced element. The contour levels range from 6% to 15% in 10 equal intervals.

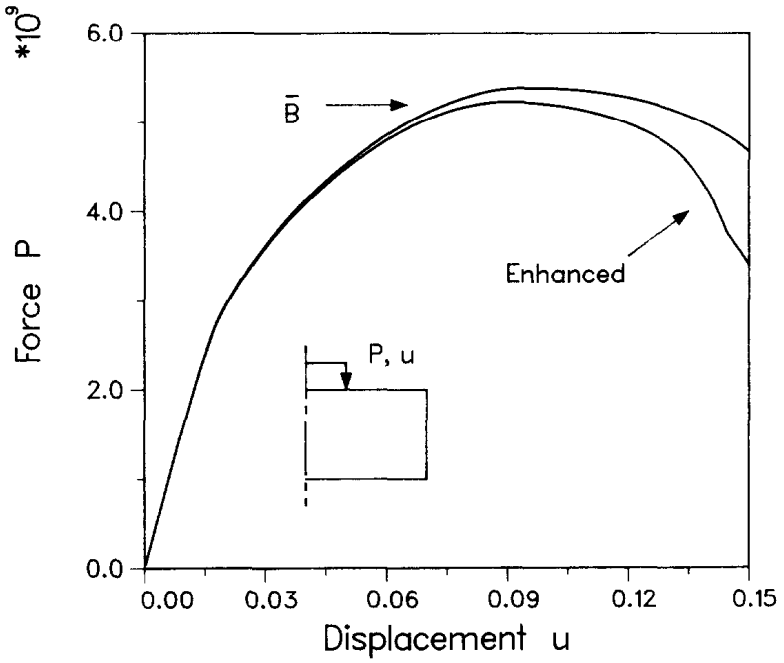

Fig. 20. Force-displacement curves.

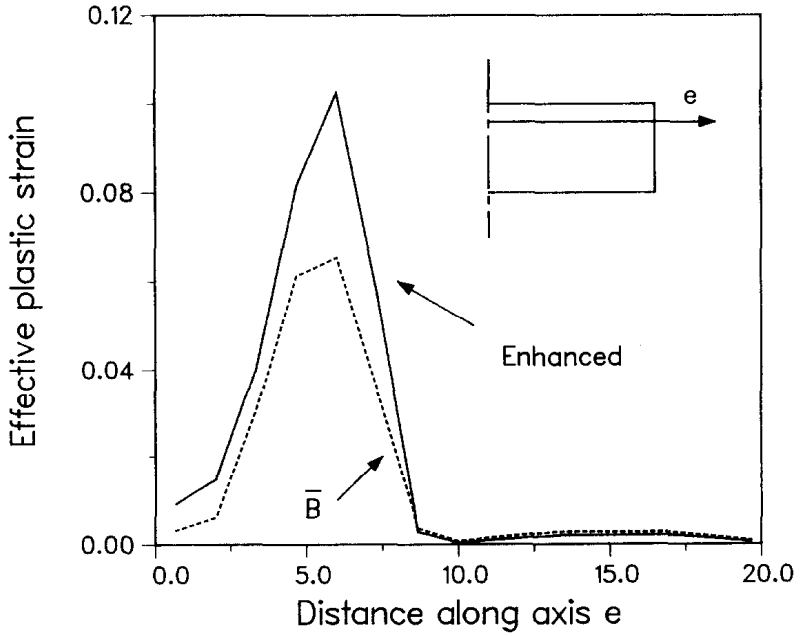

Fig. 21. Distribution of effective plastic strain across the solid.

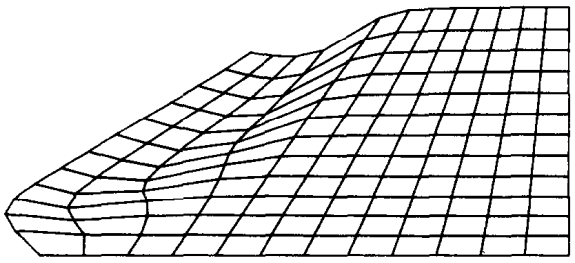

Fig. 22. Deformed mesh, displacements scaled by a factor of 1000.

the enhanced element than for the $\bar{B}$ method. The transition from diffuse to localized plastic flow involves elastic unloading towards the shear band and is delayed by the $\bar{B}$ method with respect to the enhanced element.

Our final example is concerned with a slope stability problem involving an enbankment subjected to increasing gravity loads, Fig. 22. The material model used in the calculations is Drucker–Prager's model for soils [32], with a friction angle of 20°, a dilatancy angle of 10°, and a cohesion of 2000. Perfect plasticity is assumed and the elastic response is taken to be linear and isotropic with $E = 2 \times 10^8$ and $\nu = 0.25$. This constitutive relation falls within the framework analyzed by Rudnicki and Rice [26]. A noteworthy outcome of their instability

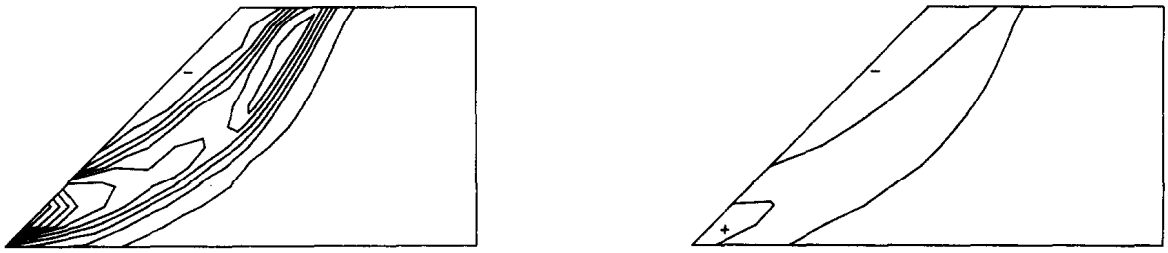

Fig. 23. Contours of effective plastic strain as computed from (a) isoparametric element and (b) enhanced element. The contour levels range from 0.0075% to 0.19% in 12 equal intervals.

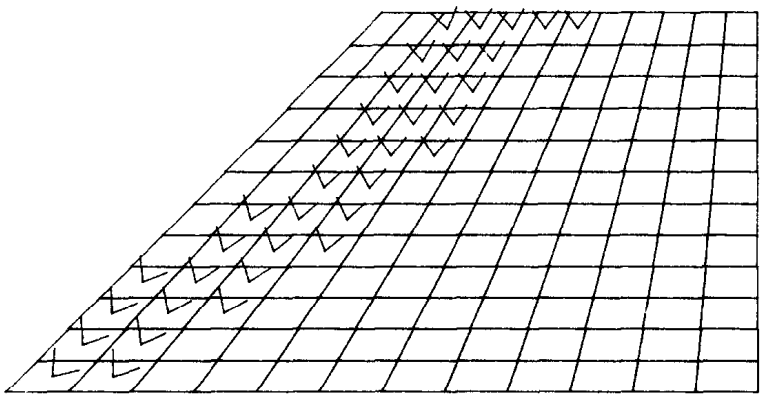

Fig. 24. Bifurcated elements and bifurcation directions.

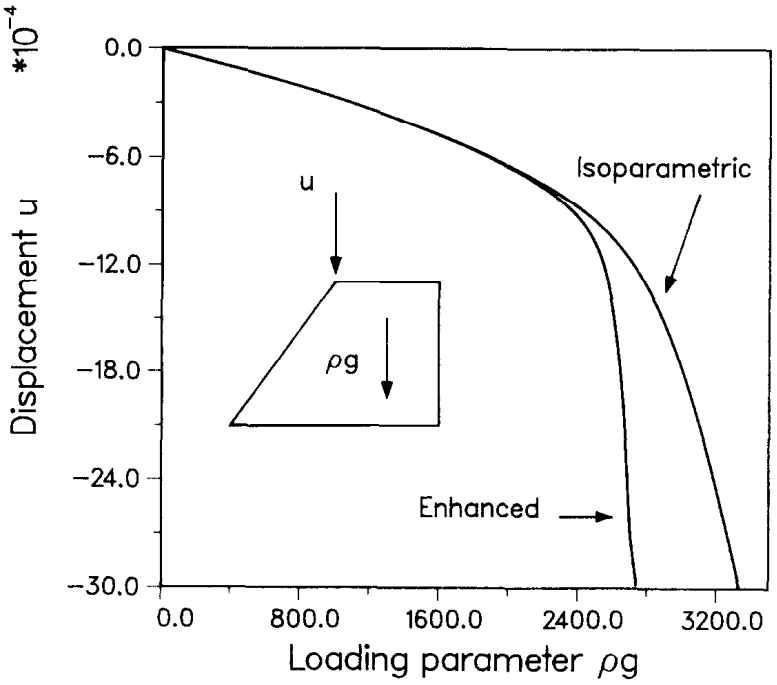

Fig. 25. Force-displacement curves.

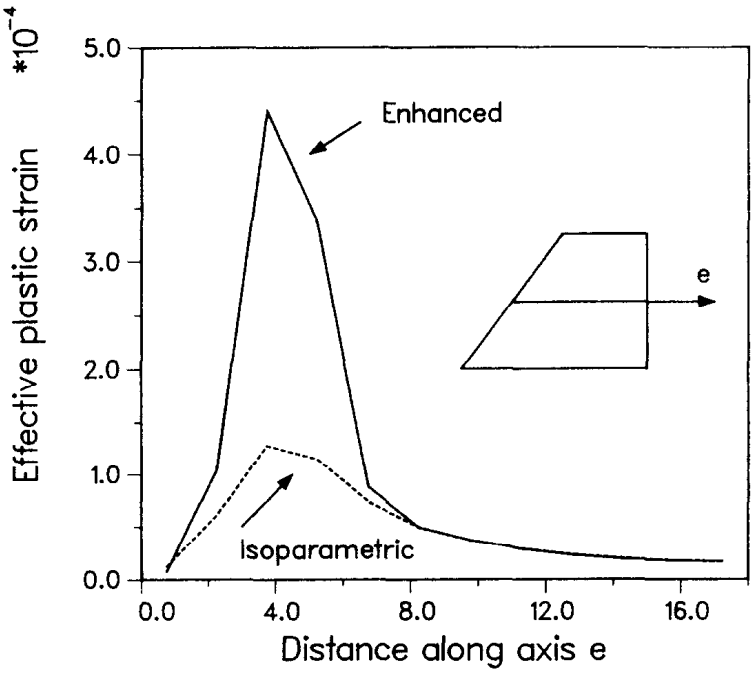

Fig. 26. Distribution of effective plastic strain across the shear band.

analysis is that the nonassociated character of the constitutive response has the effect of promoting localization. It should also be emphasized that the material under consideration is plastically dilatant and mesh locking due to near-incompressibility is of no concern. The level contours of effective plastic deformation and bifurcated elements are shown in Figs. 23 and 24. It is observed that a roughly circular shear band develops as gravity is increased. However, the isoparametric elements are seen to hinder the failure mechanism, Fig. 23(b), while the enhanced element is far more conducive to development of localized plastic deformations, Fig. 23(a). Figure 25 depicts the load-displacement curve computed by means of isoparametric and enhanced element is far more conducive to the development of localized plastic deformations, Fig. 23(a). Figure 25 depicts the load-displacement curve computed by means of isoparametric and enhanced elements. Whereas the enhanced element is seen to predict a maximum load, the isoparametric elements produce a monotonically hardening response. Since plastic flow is not incompressible, this effect cannot be attributed to mesh locking but rather to the inability of isoparametric elements to deal effectively with localized deformations. The discrepancies in the results computed from both methods are also apparent in the distribution of effective plastic strains across the shear band, Fig. 26. It is seen that the enhanced element results in levels of effective plastic strain which are four times higher than those computed from isoparametric elements.

5. Summary and conclusions

A method has been presented which aims at enhancing the performance of general classes of elements in problems involving localized failure. The method exploits the fact that considerable information concerning the process of localization can be readily obtained at the element level. A simple analysis suffices to detect the onset of localization in an element and to determine the geometry of the localized deformation modes. This information is utilized to set up additional shape functions which closely reproduce the localized deformation patterns. The additional degrees of freedom are then eliminated at the element level by static condensation. Although the resulting element is nonconforming, the patch test is satisfied and the convergence properties of the underlying conforming element are not altered. The method can be formulated as a $\bar{\boldsymbol{B}}$ method or derived directly from the Hellinger–Reissner principle. Numerical examples indicate that whereas limit loads can be accurately computed by means of finite element methods which adequately handle the incompressibility constraint, to obtain sharp predictions of localized failure modes using quadrilateral isoparametric elements further structure has to be added to the interpolation. The present approach provides an efficient means of incorporating this additional structure into general classes of 2-D and 3-D elements.

Appendix A. Solution of the localization condition

In this appendix we discuss a computational procedure for detecting the onset of localization and determining the localization directions $\boldsymbol{m}$ and $\boldsymbol{n}$. It proves convenient to treat the 2-D and 3-D cases separately.

A.1. Three-dimensional case

If the material response is path-dependent, the integration of the constitutive equations has to be carried out incrementally. If, for instance, the instantaneous initial response of the material is isotropic-elastic, the localization function (10) initially takes the value

$$f(\boldsymbol{n}) = (\lambda_0 + 2\mu_0)\mu_0^2 , \tag{A.1}$$

where λ_0 and μ_0 are the Lamé constants of the virgin material. Note that $f(\boldsymbol{n}) > 0$ and independent of $\boldsymbol{n}$. As the process of deformation progresses, f may develop minima which eventually become negative or zero. This in turn signals the onset of localization. To detect precisely when this happens, the minima of the localization function f can be computed at every deformation increment and the localization condition (10) checked at the minima. This leads to considering the constrained minimization problem,

$$\begin{aligned} &\text{minimize } f(\boldsymbol{n}) \equiv \det(n_i D_{ijkl} n_l) , \\ &\text{subject to } |\boldsymbol{n}| = 1 , \end{aligned} \tag{A.2}$$

where $\boldsymbol{D}$ is the current value of the tangent moduli. The minima are characterized by the condition

$$\frac{\partial}{\partial n_i}\left[f(\boldsymbol{n}) - \lambda|\boldsymbol{n}|^2\right] = \frac{\partial f(\boldsymbol{n})}{\partial n_i} - 2\lambda n_i = 0 , \tag{A.3}$$

where λ is a Lagrange multiplier. Differentiating f in (A.3) one obtains

$$\det(\boldsymbol{A}(\boldsymbol{n}))D_{ijkl}A^{-1}_{kj}(\boldsymbol{n})n_l - \lambda n_i = 0 . \tag{A.4}$$

Introducing the notation

$$J_{il}(\boldsymbol{n}) \equiv \det(\boldsymbol{A}(\boldsymbol{n}))D_{ijkl}A^{-1}_{kj}(\boldsymbol{n}) , \tag{A.5}$$

the minimum condition (A.4) can be recast as

$$J_{il}(\boldsymbol{n})n_l - \lambda n_i = 0 . \tag{A.6}$$

The solutions of (A.6) can be found in two steps:

(i) Expressing $\boldsymbol{n}$ in terms of spherical angles, i.e., setting $\boldsymbol{n} = (\cos\varphi\cos\theta, \cos\varphi\sin\theta, \sin\varphi)$, the range of variation $[0, 2\pi] \times [0, \frac{1}{2}\pi]$ of (θ, φ) is swept at 5-degree increments to determine a first approximation $\boldsymbol{n}^{(0)}$ to the minima.

(ii) The locations of the minima are then pinpointed by means of the iterative scheme:

$$J_{il}(\boldsymbol{n}^{(k)})n_l^{(k+1)} - \lambda^{(k+1)}n_i^{(k+1)} = 0 . \tag{A.7}$$

Thus, at every iteration an eigenvalue problem is formulated based on the matrix $\boldsymbol{J}$ evaluated

at the previous iteration $\boldsymbol{n}^{(k)}$. The minimum eigenvector of (A.7) is taken as the new iterate $\boldsymbol{n}^{(k+1)}$.

Once the orientations of the discontinuity planes have been determined, the corresponding vectors $\boldsymbol{m}$ are computed as the zero-eigenvectors of the localization matrix $\boldsymbol{A}(\boldsymbol{n})$.

A.2. Two-dimensional case

In the 2-D case the localization matrix $\boldsymbol{A}(\boldsymbol{n})$ is 2×2 and one readily finds that

$$\det(\boldsymbol{A}(\boldsymbol{n})) = a_0 n_1^4 + a_1 n_1^3 n_2 + a_2 n_1^2 n_2^2 + a_3 n_1 n_2^3 + a_4 n_2^4 , \tag{A.8}$$

where

$$\begin{aligned}
a_0 &= D_{1111}D_{1212} - D_{1112}D_{1211} ,\\
a_1 &= D_{1111}D_{1222} + D_{1111}D_{2212} - D_{1112}D_{2211} - D_{1122}D_{1211} ,\\
a_2 &= D_{1111}D_{2222} + D_{1112}D_{1222} + D_{1211}D_{2212} - D_{1122}D_{1212} - D_{1122}D_{2211} - D_{1212}D_{2211} ,\\
a_3 &= D_{1112}D_{2222} + D_{1211}D_{2222} - D_{1122}D_{2212} - D_{1222}D_{2211} ,\\
a_4 &= D_{1212}D_{2222} - D_{2212}D_{1222} .
\end{aligned} \tag{A.9}$$

Setting $n_1 = \cos\theta$, $n_2 = \sin\theta$ in (A.8) the localization condition becomes

$$f(x) = a_4 x^4 + a_3 x^3 + a_2 x^2 + a_1 x + a_0 = 0 , \tag{A.10}$$

where one writes $x = \tan\theta$. In general, the polynomial $f(x)$ in (A.10) is positive everywhere prior to localization. Thus the onset of localization can be determined by simply examining the sign of the minima of $f(x)$. These occur at the roots of the cubic polynomial $f'(x)$ which can be computed in close form by means of Cardan's formulae. As long as the minima of $f(x)$ remain positive localization does not develop. The onset of localization is signaled by one of more minima of $f(x)$ crossing the x-axis.

References

[1] Y.W. Chang and R.J. Asaro, An experimental study of shear localization in aluminum-copper single crystals, Acta Metall. 29 (1981) 241–257.

[2] L.S. Costin, E.E. Chrisman, R.H. Hawley and J. Duffy, On the localization of plastic flow in mild steel tubes under dynamic torsional loading, in: J. Harding, ed., Proceedings 2nd Conference on Mechanical Properties at High Rates of Strain, The Institute of Physics, Bristol and London, Conference Series No. 17 (1979) 90–100.

[3] T.B. Cox and J.R. Low Jr, An investigation of the plastic fracture of AISI 4340 and 18 Nickel-200 grade maraging steels, Metall. Trans. 5 (1974) 1457–1470.

[4] I. Vardoulakis, Bifurcation analysis of the triaxial test on sand samples, Acta Mech. 32 (1979) 35–54.

[5] I. Vardoulakis, Rigid granular plasticity model and bifurcation in the triaxial test, Acta Mech. 49 (1983) 57–79.

[6] W.R. Waversik and W.F. Brace, Post-failure behavior of a granite and a diabase, Rock Mech. 3 (1971) 61.

[7] J.G.M. Van Mier, Strain-softening of concrete under multiaxial loading conditions, Ph.D. Dissertation, Technische Hogeschool Eindhoven, Eindhoven, The Netherlands, 1984.

[8] J.W. Hutchinson and V. Tvergaard, Surface instabilities on statically strained plastic solids, Internat. J. Mech. Sci. 22 (1980) 339–354.
[9] M. Saje, J. Pan and A. Needleman, Void nucleation effects on shear localization in porous plastic solids, Internat. J. Fracture 17 (1982) 163–182.
[10] V. Tvergaard, A. Needleman and K.K. Lo, Flow localization in the plane strain tensile test, J. Mech. Phys. Solids 29 (2) (1981) 115–142.
[11] V. Tvergaard, Ductile fracture by cavity nucleation between larger voids, J. Mech. Phys. Solids 30 (1982) 265–286.
[12] A. Needleman and V. Tvergaard, On the finite element analysis of localized plastic deformation, in: J.T. Oden and G.F. Carey, eds., Finite Elements—Special Problems in Solid Mechanics 5 (Prentice-Hall, Englewood Cliffs, NJ, 1983) 94–157.
[13] J. Hadamard, Leçons sur la Propagation des Ondes et les Equations de L'Hydrodynamique (Hermann, Paris, 1903) Ch. 6.
[14] R. Hill, Acceleration waves in solids, J. Mech. Phys. Solids 10 (1962) 1–16.
[15] J. Mandel, Conditions de stabilité et postulat de Drucker, in: J. Kravtchenko and P.M. Sirieys, eds., Rheology and Soil Mechanics (Springer, Berlin, 1966) 58–68.
[16] T.Y. Thomas, Plastic Flow and Fracture in Solids (Academic Press, New York, 1961).
[17] J.R. Rice, The localization of plastic deformation, in: W.T. Koiter, ed., Theoretical and Applied Mechanics (North-Holland, Amsterdam, 1976) 207–220.
[18] J.H. Prevost and T.J.R. Hughes, Finite-element solution of elastic-plastic boundary value problems, ASME J. Appl. Mech. 48 (1) (1981) 69–74.
[19] J.H. Prevost, Localization of deformations in elastic-plastic solids, Internat. J. Numer. Analyt. Meths. Geomech. 8 (1984) 187–196.
[20] K.J. Willam, N. Bicanic and S. Sture, Constitutive and computational aspects of strain-softening and localization in solids, in: K.J. Willam, ed., Constitutive Equations: Macro and Computational Aspects (ASME, New York, 1984) 233–252.
[21] B.M. Irons, Numerical integration applied to finite element methods, in: Proceedings Conference on Use of Digital Computers in Structural Engineering, University of Newcastle, Newcastle, U.K., 1966.
[22] R.L. Taylor, P.J. Beresford and E.L. Wilson, A non-conforming element for stress analysis, Internat. J. Numer. Meths. Engrg. 10 (1976) 1211–1219.
[23] S.T. Pietruszcak and Z. Mroz, Finite element analysis of deformation of strain softening materials, Internat. J. Numer. Meths. Engrg. 17 (1981) 327–334.
[24] J.C. Nagtegaal, D.M. Parks and J.R. Rice, On numerically accurate finite element solutions in the fully plastic range, Comput. Meths. Appl. Mech. Engrg. 4 (1974) 153–177.
[25] T.J.R. Hughes, Generalization of selective integration procedures to anisotropic and nonlinear media, Internat. J. Numer. Meths. Engrg. 15 (1980) 1413–1418.
[26] J.W. Rudnicki and J.R. Rice, Conditions for the localization of deformation in pressure-sensitive dilatant materials, J. Mech. Phys. Solids 23 (1975) 371–394.
[27] M. Ortiz, An analytical study of the localized failure modes of concrete, Mech. Mat. (to appear).
[28] T. Belytschko and C.S. Tsay, A stabilization procedure for the quadrilateral plate element with one-point quadrature, Internat. J. Numer. Meths. Engrg. 19 (1983) 405–419.
[29] T.J.R. Hughes, W.K. Liu and A. Brooks, Review of finite element analysis of incompressible viscous flows by the penalty function formulation, J. Comput. Phys. 30 (1979) 1–60.
[30] G. Strang and G.J. Fix, An Analysis of the Finite Element Method (Prentice-Hall, Englewood Cliffs, NJ, 1973).
[31] J.C. Simo and T.J.R. Hughes, On the variational foundations of assumed strain methods, ASME J. Appl. Mech. 53 (1986) 51–54.
[32] D.C. Drucker and W. Prager, Soil mechanics and plastic analysis or limit design, Quart. J. Appl. Math. 10 (1952) 157–165.
[33] R. Hill, A general theory of uniqueness and stability in elastic-plastic solids, J. Mech. Phys. Solids 6 (1958) 236–249.
[34] B. Raniecki and O.T. Bruhns, Bounds to bifurcation stresses in solids with non-associated plastic flow laws at finite strain, J. Mech. Phys. Solids 29 (1981) 153–172.
[35] O.C. Zienkiewicz, The Finite Element Method (McGraw-Hill, New York, third ed., 1977) 280–284.